

# Ink-printed metal/graphene aerogel for glucose electro-oxidation

Alpha Chi Him Tsang<sup>1,2</sup> | Kwun Nam Hui<sup>3</sup>  | Kwan San Hui<sup>4</sup> | Biyuan Liu<sup>2</sup> | Leyi Yu<sup>2</sup> | Bin Shi<sup>2</sup> | Haibao Huang<sup>2</sup>

<sup>1</sup>Faculty of Science and Technology, Technological and Higher Education Institute of Hong Kong, Tsing Yi, Hong Kong, China

<sup>2</sup>School of Environmental Sciences and Engineering, Sun Yat-Sen University, Guangzhou, China

<sup>3</sup>Institute of Applied Physics and Materials Engineering, University of Macau, Macau, China

<sup>4</sup>School of Engineering, Faculty of Science, University of East Anglia, Norwich, UK

## Correspondence

Alpha Chi Him Tsang, Faculty of Science and Technology, Technological and Higher Education Institute of Hong Kong, Tsing Yi, Hong Kong, China.

Email: [chatsang2006@yahoo.com.hk](mailto:chtsang2006@yahoo.com.hk)

Kwun Nam Hui, Institute of Applied Physics and Materials Engineering, University of Macau, Avenida da Universidade, Macau, China.  
 Email: [bizhui@um.edu.mo](mailto:bizhui@um.edu.mo)

Kwan San Hui, School of Engineering, Faculty of Science, University of East Anglia, Norwich NR4 7TJ, UK.  
 Email: [k.hui@uea.ac.uk](mailto:k.hui@uea.ac.uk)

Haibao Huang, School of Environmental Sciences and Engineering, Sun Yat-Sen University, 510006 Guangzhou, China.  
 Email: [seabao8@gmail.com](mailto:seabao8@gmail.com)

## Abstract

Three-dimensional (3D) printing has become one of the promising technologies for the development of bulk-sized nanomaterial composites for electrocatalysis. However, traditional methods such as field deposition modeling and stereolithography are not suitable for the development of functionalized materials for practical use. A large number of studies have focused on the development of the direct ink writing (DIW) printing technique for the fabrication of graphene aerogel (GA)-based electrodes with binders for electrocatalysis. Only a few studies have focused on the synthesis of GA materials from binder-free graphene oxide (GO) using the DIW 3D printing method. Here, we describe the preparation of GA-based electrodes (without size contraction) with different Pd–Pt loadings using the DIW printing method with a commercial 3D food printer. The electron microscopy results showed that a Pd–Pt/GA monolith with a high Pd–Pt loading (59.43 wt%) could be obtained. The DIW-printed Pd–Pt/GA-2 electrode showed good electrochemical performance in glucose electrooxidation (GOR), with a high output current density of  $0.94 \text{ A g}^{-1}$  in 0.3 M glucose/1 M NaOH solution at the 3000th cycle operation (60 h). This study shows the potential of DIW-printed binder-free Pd–Pt/GA electrodes for use in fuel cell applications.

## KEY WORDS

3D printing, glucose, graphene aerogel, palladium, platinum

## 1 | INTRODUCTION

The attractive properties of graphene, such as high mechanical strength<sup>1</sup> and good electrical<sup>2</sup> and thermal conductivity,<sup>3</sup> make it a promising material for

electronic<sup>4,5</sup> and catalytic research.<sup>6–9</sup> In particular, graphene aerogel (GA)-based materials<sup>4,5,10–12</sup> have been extensively explored for energy storage and energy conversion applications. In practice, a solvothermal method was the major pathway to produce GA

This is an open access article under the terms of the Creative Commons Attribution License, which permits use, distribution and reproduction in any medium, provided the original work is properly cited.

© 2022 The Authors. *Battery Energy* published by Xijing University and John Wiley & Sons Australia, Ltd.

materials.<sup>4,5,10–12</sup> However, the GA synthesized by such a method was limited to a cylindrical shape<sup>4,5,10,11</sup> due to the surface tension of the raw graphene oxide (GO)-based solution used. Although the size and shape of scalable GA materials can be synthesized using this method, reactors with specific shapes are necessary and problems related to size contraction still exist.<sup>12</sup> Moreover, the fabricated free-standing GA materials need to be subjected to a subsequent ultrasonic treatment before their practical use<sup>5,10,13,14</sup> which could destroy the three-dimensional (3D) structure. Thus, these are the limitations in the application of GA-based materials.

The use of 3D printing techniques, including stereolithography<sup>15–18</sup> and field deposition modeling (FDM),<sup>19–21</sup> for GA synthesis has been reported by different groups in recent years. The printed GA materials have demonstrated good activity in terms of oil adsorption<sup>16</sup> and toxic dye adsorption.<sup>18</sup> However, most of the reported GA materials required the use of a surfactant<sup>19–21</sup> or lithographic resin,<sup>15–17</sup> leading to a reduction of the catalytically active sites of the GA-based materials. In addition, the preparation time for the inks is very long.<sup>19</sup> As a result, development of a direct ink writing (DIW) technique to print 3D catalyst-loaded GA-based electrodes without binders for electrocatalysis represents a new avenue of research.

In the initial years of research, an ice-supported DIW method was first demonstrated by Zhang's group to print 2.5D and 3D pure GA blocks in an aqueous GO solution, and these blocks showed comparable mechanical and electrical properties to those synthesized by traditional methods.<sup>22</sup> Then, other research groups used a scientific bioprinter or a modified FDM 3D printer with complicated ink synthesis steps<sup>22–27</sup> to print GA-based materials, which increased the overall cost and time of the printing process. Pure GA<sup>28,29</sup> and foreign material (carbon nanotube [CNT],<sup>26</sup> polymer,<sup>23</sup> metal,<sup>29</sup> monometallic oxide,<sup>30,31</sup> mixed metal oxide,<sup>32</sup> etc.)-loaded GA materials have been reported to be used in supercapacitor and lithium-ion batteries with good performance. However, most of the DIW-printed GA materials (with foreign materials) required the use of polymeric additives<sup>23</sup> or complicated fabrication steps.<sup>29–31</sup> In contrast, a few studies demonstrated the potential of a one-step DIW process for printing of CNT/GA<sup>26</sup> and G/ZnV<sub>2</sub>O<sub>6</sub>@Co<sub>3</sub>V<sub>2</sub>O<sub>6</sub><sup>32</sup> materials from catalyst/GO hybrid sol-gel solutions without the use of additives. Thus, it is important to further develop a new DIW method to print catalyst-loaded 3D GA electrodes using a low-cost commercial 3D food printer with aqueous GO-based inks.

This study reports a new DIW method to print binder-free Pd-Pt-loaded GA using an aqueous Pd-Pt-loaded GO sol-gel with a low-cost commercial 3D food printer. The Pd-Pt/GA-2 electrode has size- and

shape-scalable properties with high loading of Pd-Pt nanoparticles, showing good performance in glucose electrooxidation (GOR).

## 2 | EXPERIMENTAL SECTION

### 2.1 | Materials

The following materials and chemicals were used directly as purchased: graphite powder (325 mesh, Uni-Chem), P<sub>2</sub>O<sub>5</sub> (99%, Acros-organic), K<sub>2</sub>S<sub>2</sub>O<sub>8</sub> (99%, Fisher Scientific), KMnO<sub>4</sub> (99%, Sigma-Aldrich), H<sub>2</sub>O<sub>2</sub> (30%, Sigma-Aldrich), sulfuric acid (98%, Sigma-Aldrich), hydrochloric acid (37%, Sigma-Aldrich), K<sub>2</sub>PdCl<sub>6</sub> (99.99%, Sigma-Aldrich), and K<sub>2</sub>PtCl<sub>6</sub> (99.99%, Sigma-Aldrich).

### 2.2 | Raw GO preparation

Raw GO was synthesized using the modified Hummer's method, which has been reported elsewhere.<sup>33</sup> Briefly, 2 g of graphite powder was added to a 50 ml sulfuric acid solution containing 1 g of K<sub>2</sub>S<sub>2</sub>O<sub>8</sub> and 1 g of P<sub>2</sub>O<sub>5</sub>. The mixtures were stirred for 6 h to achieve complete mixing. The resulting solution was then rinsed and centrifuged with deionized (DI) water until the pH of the pure mixture became neutral (pH = 7). The product was then dried in an oven at 80°C overnight to remove the residual water. The dried residue obtained was preoxidized graphite oxide, which was then crushed into a powder. First, the preoxidized graphite oxide powder was added to a cold (5–10°C) sulfuric acid solution and mixed, and then 6 g of KMnO<sub>4</sub> powder was added slowly in a stepwise manner. After adding the entire KMnO<sub>4</sub> powder into the mixture solution, the temperature of the system was increased and maintained at 35°C for 2 h to achieve the second-step oxidation of the graphite oxide powder into GO. The system was quenched by the addition of 30% H<sub>2</sub>O<sub>2</sub> (10 ml) over 15 min, followed by the addition of 250 ml of DI water for rinsing and neutralizing the solution. The rinsed solution was further cleaned using 10 v/v% HCl and then centrifuged a few times to remove the residual metal ions in the raw GO suspension. The acid-cleaned raw GO was then rinsed with DI water by centrifugation to neutralize the pH of the solution to around 4–5. The rinsed GO was then further purified by dialysis tubing for 2–3 weeks with DI water for further removal of residual HCl in the mixture. The cleaned raw GO was finally freeze-dried in a freeze-drying system to remove all the water in the raw GO suspension. The spongy as-prepared GO block was then directly used without further treatment.

## 2.3 | 3D printing process

The M/GA structure was created using the modified method as reported in the literature<sup>22</sup> using the ZMorph VX food printer as shown in the Supporting Information: Figure S1. Briefly, Pd–Pt/GO ink was prepared by mixing different amounts of  $K_2PdCl_6$  (117.9 mg, 943.2 mg) and  $K_2PtCl_6$  (145.8 mg, 1166.4 mg) with 30 mg  $ml^{-1}$  GO dispersion (3 g of GO dispersed in 100 ml of DI water in an ultrasonic bath) under vigorous stirring for 30 min to obtain an aqueous Pd–Pt/GO sol–gel as shown in the Supporting Information: Figure S2, which was highly viscous even though the gel in the beaker was inverted. The Pd–Pt/GO sol–gel ink was then added to a 100 ml syringe, which was placed on the food extrusion cartridge of the 3D printer. 3D structure (2 cm × 7 cm) fabrication was achieved using the DIW method of a computer-designed pattern (Fusion 360) using a chilling plate equipped inside the printer for the bottom-up layer-by-layer formation at –30°C. Extrusion of the Pd–Pt/GO ink was achieved by the setting a layer height of 1 mm, a path width of 0.3 mm, infill speed and outline speed of 40  $mm\ s^{-1}$ , and a filament diameter of 7.15 mm in the 3D printer. The as-printed structure was further frozen in liquid nitrogen (liquid N<sub>2</sub>) for 30 min to completely freeze the product. The liquid-N<sub>2</sub> frozen Pd–Pt/GO hydrogel was then freeze-dried in a freeze-dryer for 48 h to obtain Pd–Pt/GO aerogel (GOA). The final Pd–Pt/GA was obtained by thermal reduction at 60°C in a 0.5 mg  $ml^{-1}$  vitamin C (VC) solution for 10 h, followed by vacuum freeze-drying. DIW Pd–Pt/GA with a low Pd–Pt precursor level (Pd:Pt = 117.9:145.8 mg) and a high Pd–Pt precursor level (Pd:Pt = 943.2:1166.4 mg) were denoted as Pd–Pt/GA-1 and Pd–Pt/GA-2, respectively. For comparison, pure DIW GA was also prepared using the same process, but without the addition of Pd–Pt to the GO sol–gel.

## 2.4 | Characterization

The synthesized 3D-printed Pd–Pt/GA block was characterized by transmission electron microscopy (TEM) (Philips FEI Tecnai G2 20 S-Twin Scanning TEM) and scanning electron microscopy (SEM) (Hitachi S4800 SEM) for the material morphology analysis. The elemental information of the product was obtained using energy-dispersive X-ray spectroscopy equipped with a SEM system. All metal loadings were based on SEM/EDAX by nondestructive analysis. The crystal structure of the 3D-printed Pd–Pt/GA was analyzed on the basis of the selected area electron diffraction (SAED) pattern by TEM analysis, and XRD analysis was carried out using an Ultima IV in the scanning range of 10–90°. The

Brunauer–Emmett–Teller (BET)-specific surface area of the DIW GA products was determined using a nitrogen adsorption–desorption method (Micrometrics 3Flex Physisorption). The electrochemical activity of the direct Pd–Pt/GA-1 and Pd–Pt/GA-2 electrodes was analyzed by using the CHI660E electrochemical workstation.

## 2.5 | GOR

Electrooxidation was conducted using a VC-reduced DIW Pd–Pt/GA block after cutting it into pieces 2 cm × 3.5 cm in size as shown in the Supporting Information: Figure S3. Then, it was transferred into a working electrode holder before placement in a CHI-660E electrochemical workstation. A conventional three-electrode system is commonly used in the fuel-cell electrode evaluation. In brief, DIW Pd–Pt/GA was used as a working electrode without post-treatment. A platinum plate and a standard Ag/AgCl electrode were used as a counter electrode and a reference electrode, respectively. The fuel solution for direct glucose fuel cell (DGFC) evaluation was a 0.3 M glucose/1 M NaOH solution. The scanning rate and range of the system were set at 50  $mV\ s^{-1}$  and –0.8 to +1.0 V, respectively. The reaction was carried out for 3000 cycles (60 h) at room temperature (25°C) and pressure,<sup>34</sup> and the 25th cycle result was extracted from the 3000 cycles. This parameter is commonly used in DGFC studies.<sup>35–41</sup> The mean values along with the standard deviations (within ±5%) of three sets of independent experiments are reported.

## 3 | RESULTS AND DISCUSSION

### 3.1 | DIW Pd–Pt/GA product

DIW Pd–Pt/GA was successfully synthesized by smooth extrusion of a Pd–Pt/GO hybrid filament gel from the printer as shown in the Supporting Information: Figure S4a, and the size- and shape-scalable characteristics of black DIW Pd–Pt/GA products were determined from the digital image shown in the Supporting Information: Figure S4b. Figure 1 shows the SEM images of DIW Pd–Pt/GA. Under the same magnification, the larger the amount of the Pd–Pt precursor mixed into the GO sol–gel, the higher the particle density observed in the DIW GA array (Figure 1A–D,F–I). This phenomenon was reflected in the difference between the Pt and Pd peak signal patterns in the EDAX spectra shown in Figure 1E,J, and the Pd–Pt loading levels are summarized in Table 1. In the low Pd–Pt precursor level GO sol–gel, the overall loading of Pd–Pt was only 3.3 wt%, with a low Pd:Pt atomic ratio (1:15.2) in Pd–Pt/GA-1 after VC reduction. In contrast, the overall

loading of Pd–Pt increased substantially to 59.43 wt%, with a relatively higher Pd:Pt atomic ratio (2.02:1) in Pd–Pt/GA-2 when the Pd/Pt precursor in the raw Pd–Pt/GO sol–gel was increased to eight times that in the sol–gel ink of Pd–Pt/GA-1. The possible reason for the difference in the Pd/Pt ratio (at% and wt%) in the two DIW GA products may be the difference in the reduction potential between  $\text{Pd}^{4+}$  (+0.96 V) and  $\text{Pt}^{4+}$  (+1.435 V) in the as-printed Pd–Pt/GOA, even though the Pd/Pt precursor mole ratio was the same (Pd:Pt = 1:1 [0.3:0.3 in Pd–Pt/GA-1, 2.4:2.4 in Pd–Pt/GA-2]) in two different GO hybrid sol–gels with identical GO concentrations ( $30 \text{ mg ml}^{-1}$ ). Table S1 in the Supporting Information shows that the surface area of Pd–Pt/GA-2 is  $24.37 \text{ m}^2 \text{ g}^{-1}$  with a pore size of  $0.0699 \text{ cm}^3 \text{ g}^{-1}$ , which is approximately 12 times larger than that of Pd–Pt/GA-1 (surface area:  $2.24 \text{ m}^2 \text{ g}^{-1}$ ; pore size:  $0.00582 \text{ cm}^3 \text{ g}^{-1}$ ). The results show that the higher the loading of Pd–Pt particles, the larger the BET surface area of the sample.

The Pd–Pt/GA-1 and Pd–Pt/GA-2 samples were further investigated by TEM analysis. Figures 2 and 3 show that Pd–Pt alloy NPs were successfully loaded on DIW GA arrays via one-step printing. Under an identical magnification in TEM images, the size of the Pd–Pt alloy particles on the GA was similar in the two samples. This may be because larger particles (did not adhere well properly to the GA) fell off during the preparation of the TEM samples via ultrasonication (Figure 2A–C,E–G). The blank spots on the GA samples suggest the loading of Pd–Pt alloy particles on the GA. The EDAX mapping analysis of Pd–Pt/GA samples, as shown in Figure 3, revealed that C–O pairs (Figure 3A–D) and Pd–Pt pairs (Figure 3E–H) had identical patterns, compared to the corresponding bright-field TEM image (Figure 3I–J). The results showed black spots, which were Pd–Pt alloys, and they were dispersed into GA. The crystal structure of the NPs was analyzed by the SAED pattern, as shown in Figure 2D,H. From the summarized SAED results in

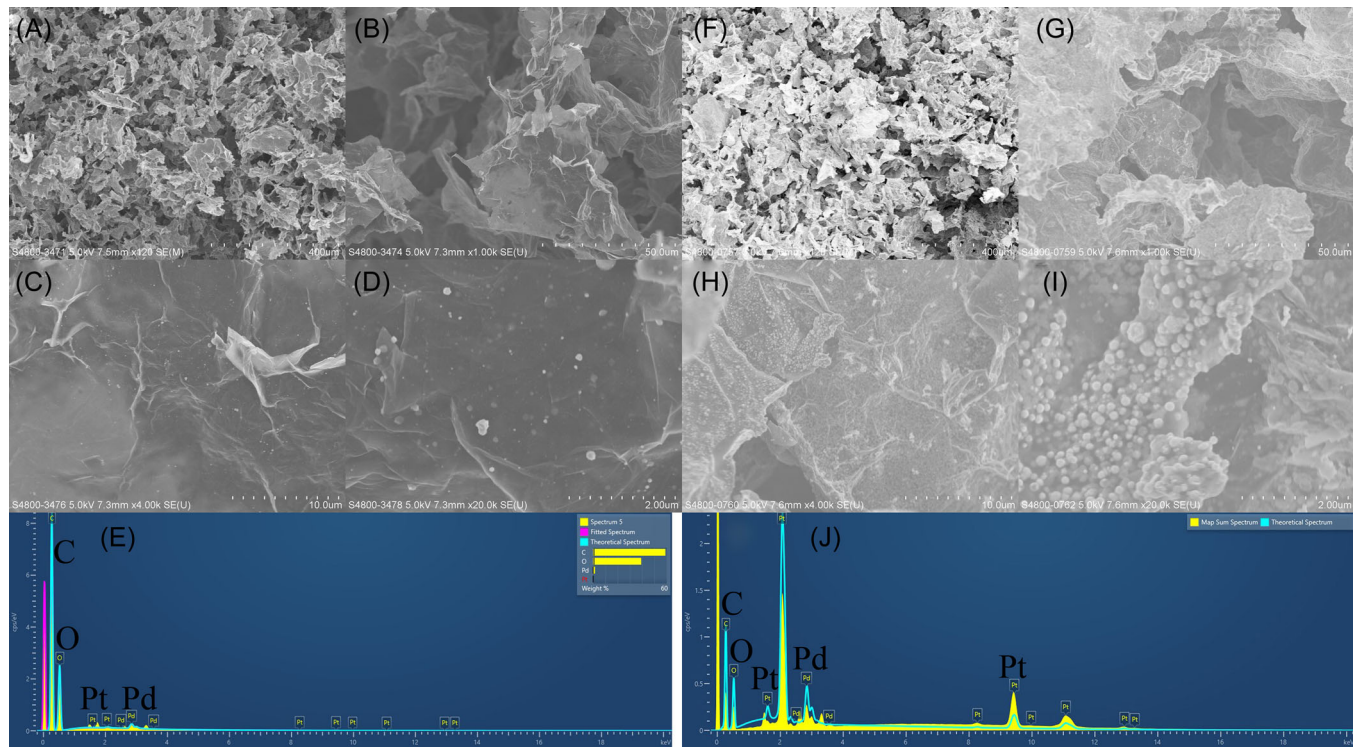


**FIGURE 1** (A–D) SEM image and (E) EDX of Pd–Pt/GA-1 and Pd–Pt/GA-2; (F–I) SEM image and (J) EDX of Pd–Pt/GA-2. Scale bar: (A, F)  $400 \mu\text{m}$ , (B, G)  $50 \mu\text{m}$ , (C, H)  $10 \mu\text{m}$ , and (D, I)  $2 \mu\text{m}$ . EDX, energy-dispersive X-ray spectroscopy; GA, graphene aerogel; SEM, scanning electron microscopy.

**TABLE 1** List of the average metal composition of the Pd–Pt/GA-1 and Pd–Pt/GA-2 electrodes (based on SEM/EDAX analysis)

Sample	Pd:Pt (mg)	Pt (at%)	Pd (at%)	Pd:Pt	Pt (wt%)	Pd (wt%)	Total loading (wt%)
Pd–Pt/GA-1	117.9:145.8	0.025	0.38	1:15.2	0.33	2.93	3.26
Pd–Pt/GA-2	943.2:1166.4	6.97	3.45	2.02:1	46.78	12.65	59.43

Abbreviations: EDAX, energy-dispersive X-ray spectroscopy; GA, graphene aerogel; SEM, scanning electron microscopy.

Table 2, it is clear that three spots in Pd–Pt/GA-1 reflected the crystal faces of (111) (spot 1), (200) (spot 2), and (220) (spot 3) (Figure 2D), and eight spots in Pd–Pt/GA-2 reflected the crystal faces of (111) (spot 1), (200) (spots 2 and 3), (220) (spot 4), (311) (spots 5 and 6), (222) (spot 7), and (400) (spot 8) (Figure 2H), respectively. The *d*-spacing was very close to or between that of pure Pd and Pt, which indicates that the black nanoparticles in TEM images were Pd–Pt alloy by

nature with the f–c–c arrangement in DIW Pd–Pt/GA monoliths.

The crystal structure of particles and the reduction of GO in DIW Pd–Pt/GA products were investigated by XRD measurement as shown in the Supporting Information: Figure S5. Figure S5a in the Supporting Information shows the presence of M (111), M (200), M (220), and M (311) peaks, which generally matched the microscopic

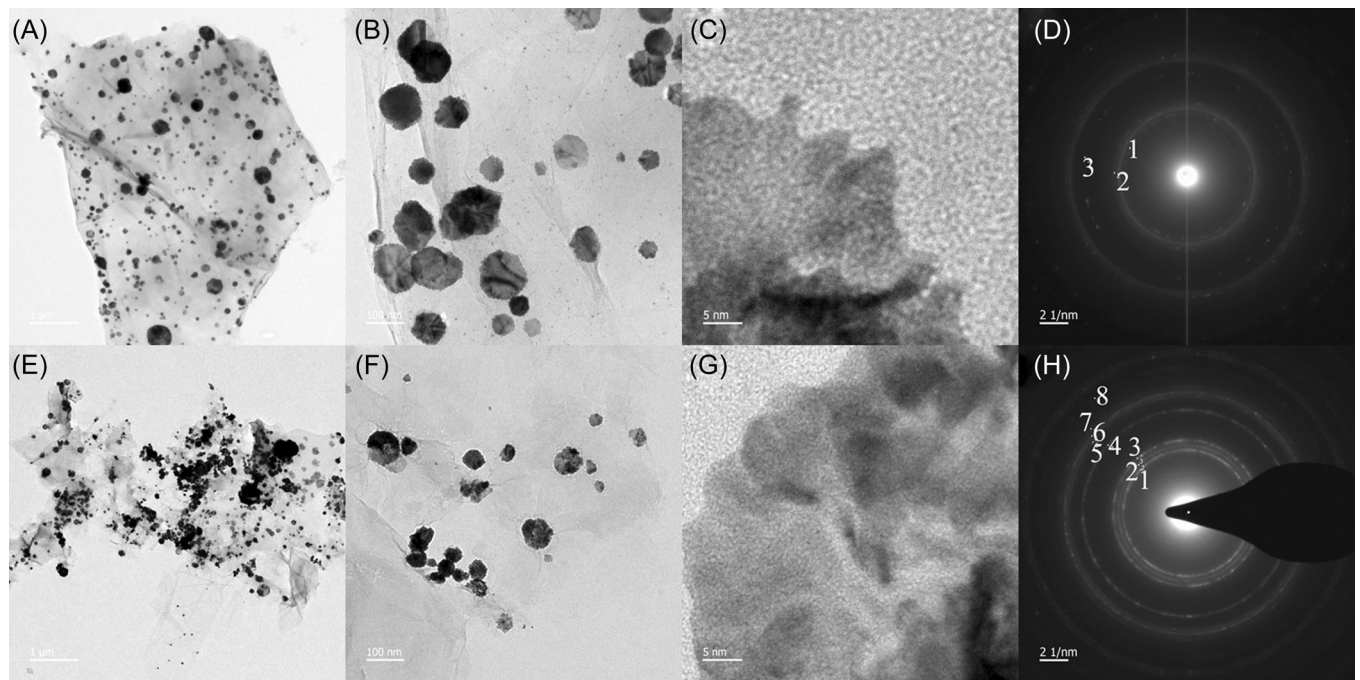


**FIGURE 2** (A–C) TEM image and (D) SAED pattern of Pd–Pt/GA-1, and (E–G) TEM image and (H) SAED pattern and Pd–Pt/GA-2. Scale bar: (A, E) 1  $\mu$ m, (B, F) 100 nm, (C, G) 5 nm, and (D, H) 2 1/nm. EDX, energy-dispersive X-ray spectroscopy; GA, graphene aerogel; SAED, selected area electron diffraction; TEM, transmission electron microscopy.

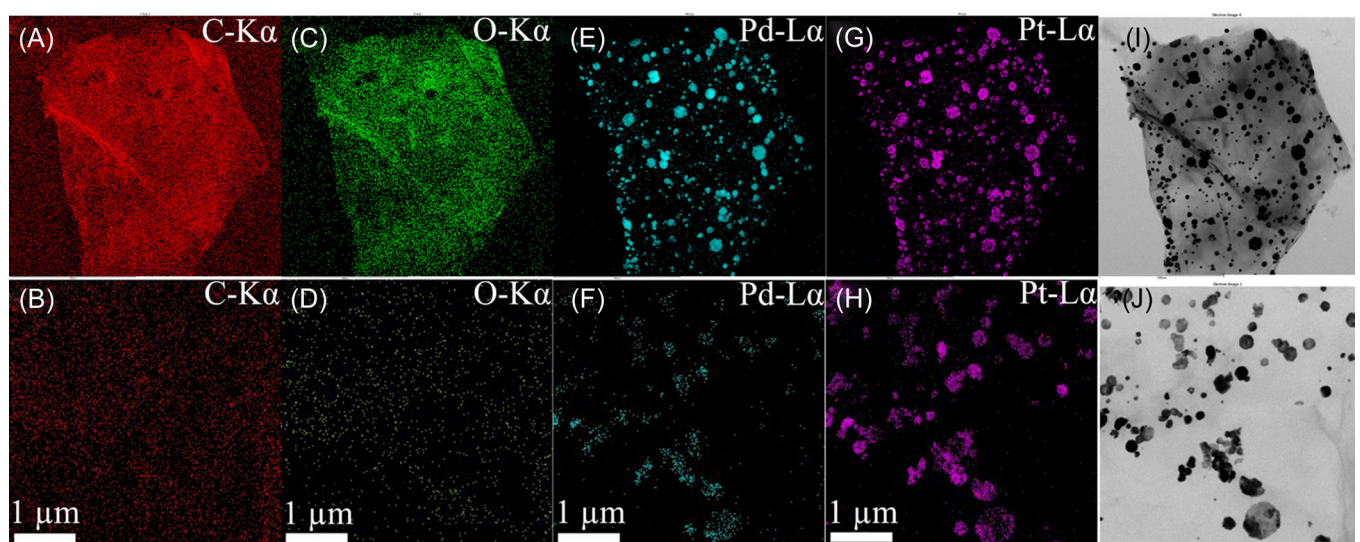


**FIGURE 3** Elemental mapping pattern (A, B) C-K $\alpha$ , (C, D) O-K $\alpha$ , (E, F) Pd-L $\alpha$ , (G, H) Pt-L $\alpha$ , and (I, J) corresponding TEM image of Pd–Pt/GA-1 and Pd–Pt/GA-2. Scale bar: (A, C, E, G, H) 500 nm; (B, D, F, H, J) 1  $\mu$ m. GA, graphene aerogel; TEM, transmission electron microscopy.

results of the Pd–Pt crystal structure via SAED analysis (Figure 2D,H). The zoomed-in result (Supporting Information: Figure S5b) shows that the M (111) peak in Pd–Pt/GA-2 was located at a higher  $2\theta$  value relative to Pd–Pt/GA-1. According to the atomic loading ratio of Pd/Pt

(Table 2), the ratio in Pd–Pt/GA-1 is larger than that of Pd–Pt/GA-2 (1:15.2 vs. 2.02:1), with the shifting of the  $2\theta$  value to a higher value ( $40.22^\circ$  vs.  $40.225^\circ$ ), and the recorded M (111) in the current samples shifted from that of the pure Pd and Pt M (111) peaks' reference positions

**TABLE 2** *d*-spacing, angles, and corresponding face of the SAED pattern of Pd–Pt NPs in Pd–Pt/GA-1 and Pd–Pt/GA-2 versus pure Pd and Pt from the built-in database of the TEM based on Figure 2

Sample	Spot	<i>d</i> -spacing (Å)	Degree to spot 1	Face ( <i>h, k, l</i> )
Pd–Pt/GA-1	1	2.660	0	111
	N/A	2.4458 (Pd)	N/A	111
	N/A	2.265 (Pt)	N/A	111
	2	1.975	23.49	200
	N/A	1.9451 (Pd)	N/A	200
	N/A	1.9616 (Pt)	N/A	200
	3	1.385	15.75	220
	N/A	1.3753 (Pd)	N/A	220
	N/A	1.3873 (Pt)	N/A	220
Pd–Pt/GA-2	1	2.554	0	111
	N/A	2.4458 (Pd)	N/A	111
	N/A	2.265 (Pt)	N/A	111
	2	2.099	2.20	200
	N/A	1.9451 (Pd)	N/A	200
	N/A	1.9616 (Pt)	N/A	200
	3	1.939	5.08	200
	N/A	1.9451 (Pd)	N/A	200
	N/A	1.9616 (Pt)	N/A	200
	4	1.376	1.58	220
	N/A	1.3753 (Pd)	N/A	220
	N/A	1.3873 (Pt)	N/A	220
	5	1.216	5.14	311
	N/A	1.1729 (Pd)	N/A	311
	N/A	1.1826 (Pt)	N/A	311
	6	1.171	3.06	311
	N/A	1.1729 (Pd)	N/A	311
	N/A	1.1826 (Pt)	N/A	311
	7	1.123	0.85	222
	N/A	1.1229 (Pd)	N/A	222
	N/A	1.1325 (Pt)	N/A	222
	8	0.9769	9.24	400
	N/A	0.9725 (Pd)	N/A	400
	N/A	0.9808 (Pt)	N/A	400

Abbreviations: GA, graphene aerogel; N/A, not available; NP, nanoparticle; SAED, selected area electron diffraction; TEM, transmission electron microscopy.

according to the JPCDS card position (Pd: 40–1043; Pt: 04–0802). Furthermore, the presence of a peak at  $12.10^\circ$  in Pd–Pt/GA-1 and at  $13.05^\circ$  in Pd–Pt/GA-2 (Supporting Information: Figure S5a) reflected the reduction of GO into reduced GO.<sup>34,42</sup> These results were similar to those found in similar materials synthesized using the conventional method as reported in our previous study.<sup>34,42</sup> The results suggested f-c-c structured Pd–Pt alloy nanoparticle formation throughout the DIW printing process and a chemical reduction of DIW Pd–Pt/GOA.

Elemental information of DIW products was further obtained by X-ray photoelectron spectroscopy (XPS) analysis, as shown in Figure 4. The appearance of Pd and Pt signals in the survey spectra of DIW Pd–Pt/GA (Figure 4A,B) reflected the presence of Pd–Pt NPs in the DIW products. Further

analysis from the high-resolution XPS recorded in Figure 4C–H is summarized as follows. In the C1s of two samples (Figure 4C,D), the intensities of –C–O–C– peaks (286.2–286.9 eV) and O=C–OH peak (288–289.2 eV) were much weaker than that of the C–C sp<sup>2</sup> peak (284.2–284.8 eV), which was concrete evidence of GO reduction by VC solution under mild conditions. A clear pattern of Pt and Pd peaks in Pt4f spectra (Figure 4E,F) and Pd3d spectra (Figure 4G,H) reflected the appearance of Pt<sup>0</sup> (70.7–71.45 eV, 74–74.75 eV) and Pt<sup>2+</sup> (71.9–72.45 eV, 75.5–75.95 eV) twin peak pairs, and Pd<sup>0</sup> (335.2–335.65 eV, 340.5–340.9 eV) and Pd<sup>2+</sup> (335.2–336.65 eV, 342.5–342.7 eV) twin peak pairs. Combined with XRD results (Supporting Information: Figure S5), the results suggest f-c-c Pd–Pt NPs with reduced graphene in the DIW

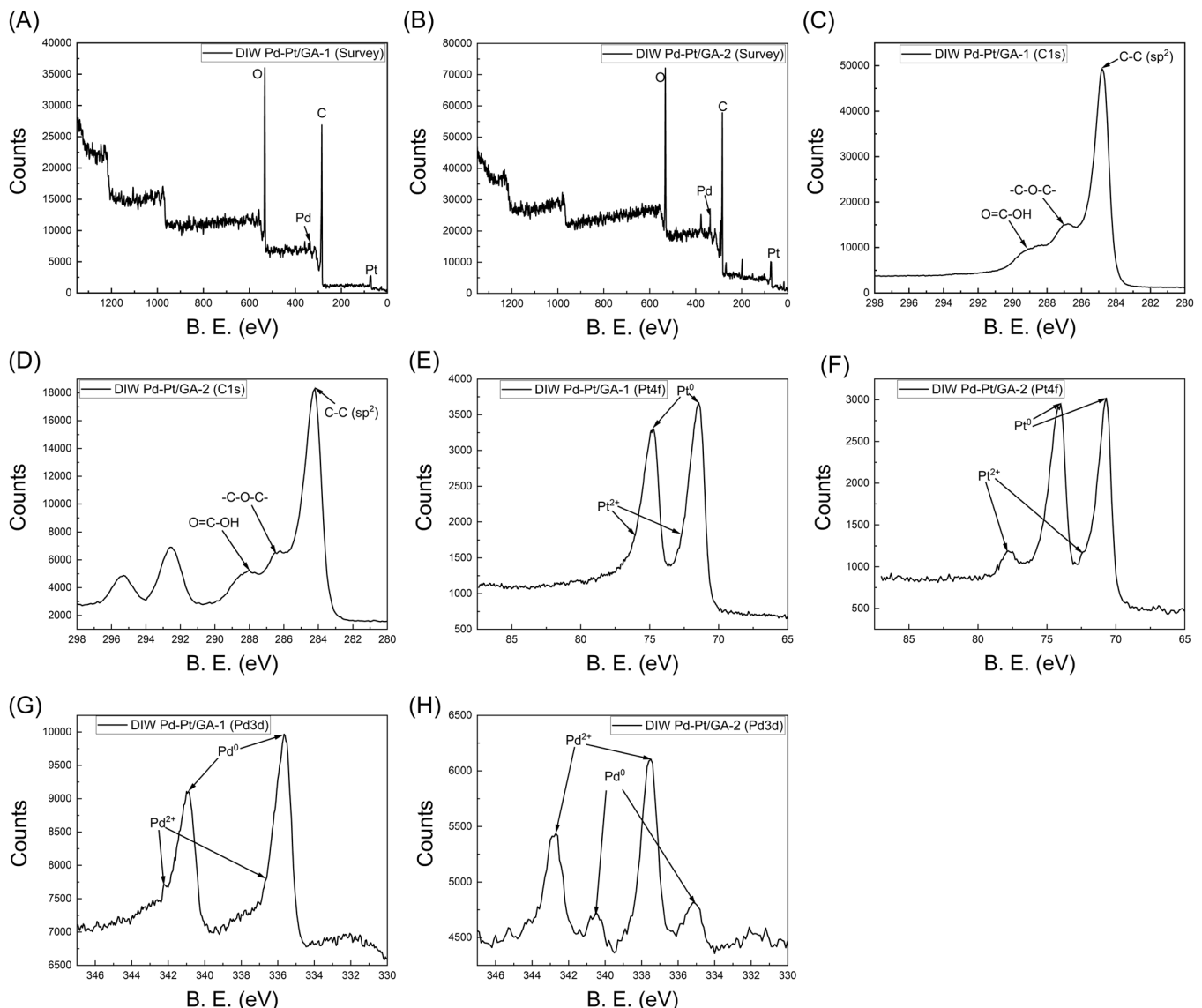


**FIGURE 4** XPS spectra of Pd–Pt/GA-1 and Pd–Pt/GA-2: (A, B) Survey and high-resolution XPS: (C, D) C1s, (E, F) Pt4f, and (G, H) Pd3d. GA, graphene aerogel; XPS, X-ray photoelectron spectroscopy.

GA arrays, showing the successful reduction of Pd/Pt binary precursors into metallic Pd/Pt with GO in VC solution simultaneously. The results show the potential of one-step additive-free DIW of Pd–Pt/GA without the use of cross-linkers or additives. The problem of size contraction and the requirement of the use of a specific reactor in the synthesis of GA can also be eliminated (Supporting Information: Figure S4b).

### 3.2 | GOR activity of binder-free DIW Pd–Pt/GA

DIW-printed Pd–Pt/GA electrodes in a fixed alkaline glucose fuel solution (0.3 M glucose/1 M NaOH) were

investigated for GOR. The half-cell activity operation for 60 h (3000 cycles) at room temperature (25°C) was conducted to measure the electrochemical performance of the electrodes. From the cyclic voltammetry (CV) curves measured at the 25th cycle of the GOR operation (Figure 5A–C), the normalized CV results with respect to the mass of active catalysts (Figure 5A) showed no obvious peak in the DIW-printed pure GA, while a weak peak at +0.16 V appeared at the 25th cycle (Figure 5C) with a current density of 1.79 A g<sup>-1</sup> in the Pd–Pt/GA-1 system. The current density recorded in the Pd–Pt/GA-2 system at +0.16 V was 2.46 A g<sup>-1</sup>, which was approximately 1.4 times larger than that of the Pd–Pt/GA-1 system. A high Pd–Pt loading in Pd–Pt/GA-2 provided more active catalysts

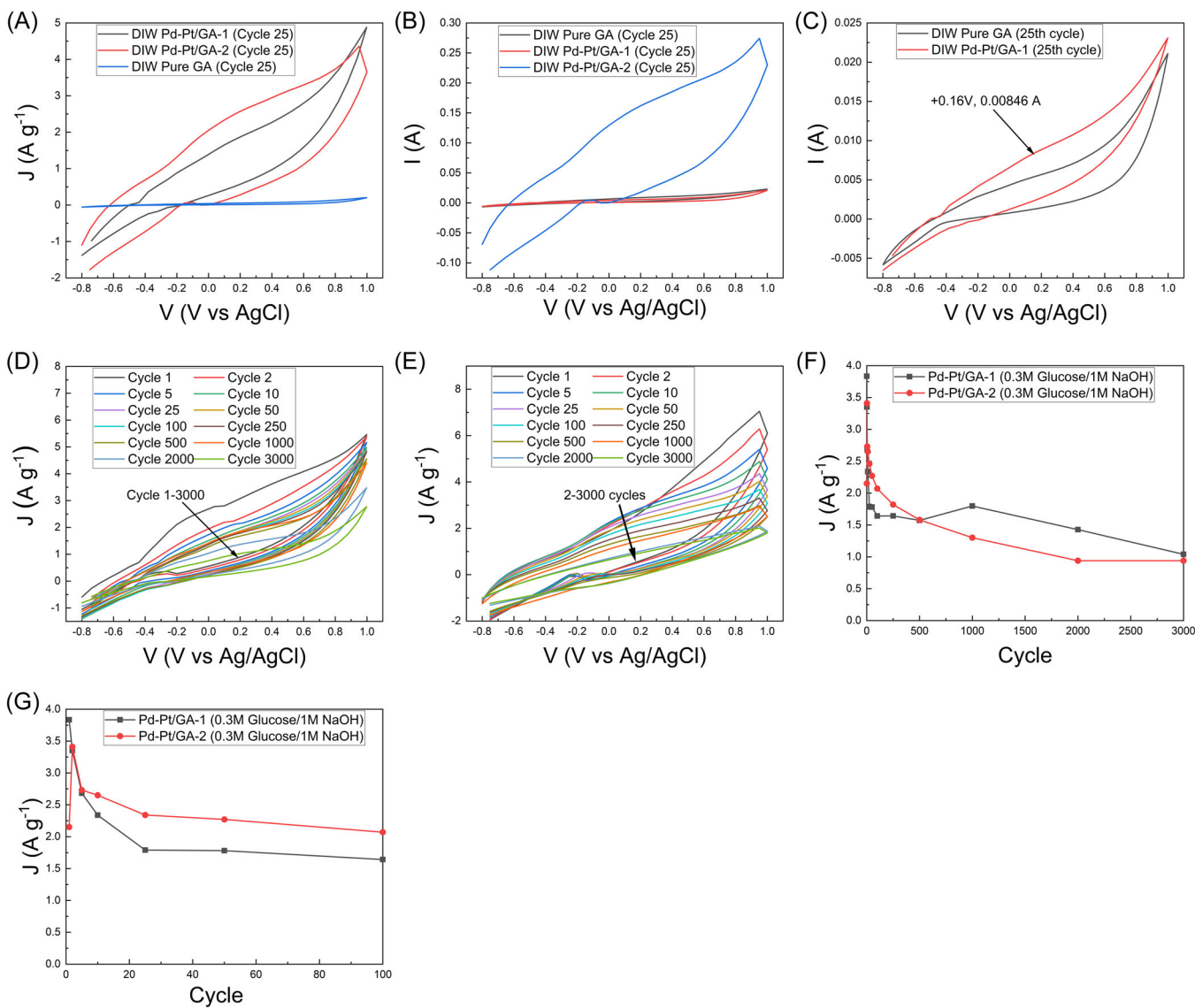


**FIGURE 5** CV results of normalized GOR by Pd–Pt/GA-1 and Pd–Pt/GA-2 versus pure GA at (A) the 25th cycle and (B) non-normalized CV results of the corresponding analysis at the 25th cycle and (C) zoomed-up region of Pd–Pt/GA-1 versus pure GA; (D, E) CV curve, (F)  $J_f$  variation of Pd–Pt/GA-1 and Pd–Pt/GA-2 throughout 3000 cycles of the GOR operation, and (G) zoomed-up region of the first 100 cycles. CV, cyclic voltammetry; GA, graphene aerogel; GOR, glucose electrooxidation.

**TABLE 3** Variation of  $J_f$  throughout 3000 cycles of GOR based on Figure 5F,G

Cycle	Pd-Pt/GA-1		Pd-Pt/GA-2	
	$J_f$ ( $\text{A g}^{-1}$ )	$J_f/J_{\text{Max}}$	$J_f$ ( $\text{A g}^{-1}$ )	$J_f/J_{\text{Max}}$
1	3.83	1	2.15	0.630
2	3.35	0.875	3.41	1
5	2.68	0.699	2.73	0.801
10	2.34	0.611	2.65	0.777
25	1.79	0.467	2.46	0.721
50	1.78	0.465	2.27	0.666
100	1.64	0.428	2.07	0.607
250	1.64	0.428	1.82	0.534
500	1.57	0.410	1.58	0.463
1000	1.80	0.470	1.30	0.381
2000	1.43	0.373	0.94	0.276
3000	1.04	0.272	0.94	0.276

Abbreviations: GA, graphene aerogel; GOR, glucose electrooxidation.

for GOR (Table 1). Figure 5B,C shows that the DIW pure GA shows no activity.

Figure 5D-G and Table 3 show that the Pd-Pt/GA-1 and the Pd-Pt/GA-2 electrodes were first activated (at the 10th cycle) and then the current density ( $J_f$ ) gradually decreased over the 3000 cycles. As shown in Table 3, the decrease in the  $J_f$  value of the Pd-Pt/GA-2 electrode is less than that of the Pd-Pt/GA-1 electrode at the 100th cycle (39.7% vs. 57.2%) and the 3000th cycle (72.4% vs. 72.8%), suggesting that the electrochemical stability of the Pd-Pt/GA-2 electrode is better than that of the Pd-Pt/GA-1 electrode. This observation was indicative of further development of the binder-free DIW-printed Pd-Pt loaded GA electrodes for the liquid phase or moist gas-phase energy conversion systems, including solid oxide fuel cell and fuel cell batteries.

## 4 | CONCLUSION

Free-standing, additive-free Pd-Pt/GA electrodes without size contraction were successfully synthesized using the one-step DIW method with a Pd-Pt/GO hybrid sol-gel. The results showed that the Pd-Pt loadings (wt%) on the DIW Pd-Pt/GA samples could be tuned by changing the amount of Pd and Pt precursors. The Pd-Pt/GA-2 electrode showed good performance in GOR throughout the 3000 cycles (60 h) (only 39.3% of the output current density depreciation

with respect to the 100th cycle). This study may provide a new strategy for the preparation of binder-free DIW-printed GA-based electrodes for electrocatalysis in energy conversion and energy storage applications.

## ACKNOWLEDGMENTS

This study was supported by a grant from the Hong Kong-Scotland Partners in Post Doctoral Research Scheme under the Research Grants Council of Hong Kong and the Scotland Government (S-HKU702/15), the Natural Science Foundation of China (NSFC) and the Research Grants Council (RGC) of Hong Kong Joint Research Scheme (Nos. 51561165015 and N\_HKU718/15), NSFC (21677179), the Guangdong Special Fund for Science & Technology Development (Hong Kong Technology Cooperation Funding Scheme) (No. 2016A050503022), the Innovation Platform Construction of Guangdong and Hong Kong (No. 2017B050504001), the Guangzhou Science and Technology Project (No. 201504301654288), the Key Fundamental Research Fund for the Central Universities (17lgjc17), the National Key Research and Development Program of China (No. 2016YFC0204800), and University of Macau (MYRG2018-00192-IAPME).

## CONFLICT OF INTEREST

The authors declare no conflict of interest.

## DATA AVAILABILITY STATEMENT

Data are available on request from the authors.

## ORCID

Kwun Nam Hui  <http://orcid.org/0000-0002-3008-8571>

## REFERENCES

- Zhu Y, Murali S, Cai W, et al. Graphene and graphene oxide: synthesis, properties, and applications. *Adv Mater.* 2010; 22(35):3906-3924.
- Lee C, Wei X, Kysar JW, Hone J. Measurement of the elastic properties and intrinsic strength of monolayer graphene. *Science.* 2008;321(5887):385-388.
- Balandin AA, Ghosh S, Bao W, et al. Superior thermal conductivity of single-layer graphene. *Nano Lett.* 2008;8(3): 902-907.
- Wu ZS, Winter A, Chen L, et al. Three-dimensional nitrogen and boron co-doped graphene for high-performance all-solid-state supercapacitors. *Adv Mater.* 2012;24(37):5130-5135.
- Sui ZY, Meng YN, Xiao PW, Zhao ZQ, Wei ZX, Han BH. Nitrogen-doped graphene aerogels as efficient supercapacitor electrodes and gas adsorbents. *ACS Appl Mater Interfaces.* 2015;7(3):1431-1438.
- Kim SH, Jeong GH, Choi D, et al. Synthesis of noble metal/graphene nanocomposites without surfactants by one-step reduction of metal salt and graphene oxide. *J Colloid Interface Sci.* 2013;389:85-90.

7. Gao YJ, Ma D, Wang CL, Guan J, Bao XH. Reduced graphene oxide as a catalyst for hydrogenation of nitrobenzene at room temperature. *Chem Commun.* 2011;47(8):2432-2434.
8. Sui Z, Zhang X, Lei Y, Luo Y. Easy and green synthesis of reduced graphite oxide-based hydrogels. *Carbon.* 2011;49(13):4314-4321.
9. Zhu Y, Murali S, Stoller MD, et al. Carbon-based supercapacitors produced by activation of graphene. *Science.* 2011;332(6037):1537-1541.
10. Ren L, Hui KS, Hui KN. Self-assembled free-standing three-dimensional nickel nanoparticle/graphene aerogel for direct ethanol fuel cells. *J Mater Chem A.* 2013;1(18):5689-5694.
11. Hou C, Zhang Q, Li Y, Wang H. P25-graphene hydrogels: room-temperature synthesis and application for removal of methylene blue from aqueous solution. *J Hazard Mater.* 2012;205-206:229-235.
12. Worsley MA, Charnvanichborikarn S, Montalvo E, et al. Toward macroscale, isotropic carbons with graphene-sheet-like electrical and mechanical properties. *Adv Funct Mater.* 2014;24(27):4259-4264.
13. Kung CC, Lin PY, Xue Y, et al. Three dimensional graphene foam supported platinum–ruthenium bimetallic nanocatalysts for direct methanol and direct ethanol fuel cell applications. *J Power Sources.* 2014;256:329-335.
14. Krittayavathananon A, Sawangphruk M. Electrocatalytic oxidation of ethylene glycol on palladium coated on 3D reduced graphene oxide aerogel paper in alkali media: effects of carbon supports and hydrodynamic diffusion. *Electrochim Acta.* 2016;212:237-246.
15. Lin D, Jin S, Zhang F, et al. 3D stereolithography printing of graphene oxide reinforced complex architectures. *Nanotechnology.* 2015;26(43):404003.
16. Zhang QQ, Zhang F, Xu X, Zhou C, Lin D. Three-dimensional printing hollow polymer template-mediated graphene lattices with tailororable architectures and multifunctional properties. *ACS Nano.* 2018;12(2):1096-1106.
17. Wang D, Huang X, Li J, et al. 3D printing of graphene-doped target for “matrix-free” laser desorption/ionization mass spectrometry. *Chem Commun.* 2018;54(22):2723-2726.
18. Zhou G, Wang KP, Liu HW, et al. Three-dimensional polylactic acid@graphene oxide/chitosan sponge bionic filter: highly efficient adsorption of crystal violet dye. *Int J Biol Macromol.* 2018;113:792-803.
19. Wei X, Li D, Jiang W, et al. 3D printable graphene composite. *Sci Rep.* 2015;5:11181.
20. Zhang D, Chi B, Li B, et al. Fabrication of highly conductive graphene flexible circuits by 3D printing. *Synth Metals.* 2016;217:79-86.
21. Foster CW, Down MP, Zhang Y, et al. 3D printed graphene based energy storage devices. *Sci Rep.* 2017;7:42233.
22. Zhang QQ, Zhang F, Medarametla SP, Li H, Zhou C, Lin D. 3D printing of graphene aerogels. *Small.* 2016;12(13):1702-1708.
23. Tang X, Zhou H, Cai Z, et al. Generalized 3D printing of graphene-based mixed-dimensional hybrid aerogels. *ACS Nano.* 2018;12(4):3502-3511.
24. Huang K, Yang J, Dong S, et al. Anisotropy of graphene scaffolds assembled by three-dimensional printing. *Carbon.* 2018;130:1-10.
25. Tubio CR, Rama A, Gomez M, del Rio F, Guitian F, Gil A. 3D-printed graphene-Al<sub>2</sub>O<sub>3</sub> composites with complex mesoscale architecture. *Ceram Int.* 2018;44(5):5760-5767.
26. Wang Z, Zhang Q, Long S, et al. Three-dimensional printing of polyaniline/reduced graphene oxide composite for high-performance planar supercapacitor. *ACS Appl Mater Interfaces.* 2018;10(12):10437-10444.
27. Ma J, Wang P, Dong L, Ruan Y, Lu H. Highly conductive, mechanically strong graphene monolith assembled by three-dimensional printing of large graphene oxide. *J Colloid Interface Sci.* 2019;534:12-19.
28. Jiang Y, Xu Z, Huang T, et al. Direct 3D printing of ultralight graphene oxide aerogel microlattices. *Adv Funct Mater.* 2018;28(16):1707024.
29. Lacey SD, Kirsch DJ, Li Y, et al. Extrusion-based 3D printing of hierarchically porous advanced battery electrodes. *Adv Mater.* 2018;30(12):1705651.
30. Yao B, Chandrasekaran S, Zhang J, et al. Efficient 3D printed pseudocapacitive electrodes with ultrahigh MnO<sub>2</sub> loading. *Joule.* 2019;3(2):459-470.
31. Wang T, Li L, Tian X, et al. 3D-printed interdigitated graphene framework as superior support of metal oxide nanostructures for remarkable micro-pseudocapacitors. *Electrochim Acta.* 2019;319:245-252.
32. Zhao J, Zhang Y, Zhao X, et al. Direct ink writing of adjustable electrochemical energy storage device with high gravimetric energy densities. *Adv Funct Mater.* 2019;29(26):1900809.
33. Kovtyukhova NI, Ollivier PJ, Martin BR, et al. Layer-by-layer assembly of ultrathin composite films from micron-sized graphite oxide sheets and polycations. *Chem Mat.* 1999;11(3):771-778.
34. Tsang CHA, Hui KN, Hui KS. Influence of Pd<sub>1</sub>Pt<sub>x</sub> alloy NPs on graphene aerogel/nickel foam as binder-free anodic electrode for electrocatalytic ethanol oxidation reaction. *J Power Sources.* 2019;413:98-106.
35. Becerik I. The role of electrolytically co-deposited platinum–palladium electrodes on the electrooxidation of D glucose in alkaline medium: a synergistic effect. *Turk J Chem.* 1999;23(1):57-66.
36. Becerik I, Suzer S, Kadirgan F. Platinum–palladium loaded polypyrrole film electrodes for the electrooxidation of D-glucose in neutral media. *J Electroanal Chem.* 1999;476:171-176.
37. Spets JP, Lampinen MJ, Kiros Y, Rantanen J, Anttila T. Direct glucose fuel cell with the anion exchange membrane in the near-neutral-state electrolyte. *Int J Electrochem Sci.* 2012;7(12):11696-11705.
38. Das D, Ghosh S, Basumallick I. Electrochemical studies on glucose oxidation in an enzymatic fuel cell with enzyme immobilized on to reduced graphene oxide surface. *Electroanalysis.* 2014;26(11):2408-2418.
39. An L, Zhao TS, Shen SY, Wu QX, Chen R. Alkaline direct oxidation fuel cell with non-platinum catalysts capable of

- converting glucose to electricity at high power output. *J Power Sources*. 2011;196(1):186-190.
40. Cai ZX, Liu CC, Wu GH, Chen XM, Chen X. Palladium nanoparticles deposit on multi-walled carbon nanotubes and their catalytic applications for electrooxidation of ethanol and glucose. *Electrochim Acta*. 2013;112:756-762.
41. Brouzgou A, Yan LL, Song SQ, Tsiaikaras P. Glucose electrooxidation over  $Pd_xRh/C$  electrocatalysts in alkaline medium. *Appl Catal B*. 2014;147:481-489.
42. Tsang CHA, Hui KN, Hui KS. Electrooxidation of glucose by binder-free bimetallic  $Pd_1Pt_x$ /graphene aerogel/nickel foam composite electrodes with low metal loading in basic medium. *Electrochim Acta*. 2017;258:371-379.

**SUPPORTING INFORMATION**

Additional supporting information can be found online in the Supporting Information section at the end of this article.

**How to cite this article:** Tsang ACH, Hui KN, Hui KS, et al. Ink-printed metal/graphene aerogel for glucose electro-oxidation. *Battery Energy*. 2022;1:20220004. doi:10.1002/bte.20220004